Applied Thermal Engineering 301 (2026) 131680

Contents lists available at ScienceDirect

Applied Thermal Engineering

journal homepage: www.elsevier.com/locate/ate

Research Paper

Analysis of heat transport mechanisms in packed-bed thermal energy storage using liquid metal as heat transfer fluid and simulation of a lab-scale experiment☆

Eike A. Schmidt *, Thomas Wetzel, Klarissa Niedermeier *

Karlsruhe Institute of Technology (KIT), Institute for Thermal Energy Technology and Safety (ITES), Hermann-von-Helmholtz-Platz 1, Eggenstein-Leopoldshafen, 76344, Germany

ARTICLE INFO

Keywords:
Thermal energy storage
Liquid metals
Packed bed
Heat transfer
Effective thermal conductivity

ABSTRACT

Thermal energy storage (TES) systems are a crucial component of pumped thermal energy storage systems, so-called Carnot Batteries, and are expected to play an important role in the energy transition. As a possible TES configuration, a packed-bed with liquid metal as a heat transfer fluid has been proposed. To optimize and further investigate this concept, simulations of the thermocline propagation in the packed-bed TES are required. For this purpose, one-dimensional heterogeneous continuum models are frequently used. The heat transport mechanisms and the effective transport parameters needed for these models have been extensively studied for conventional fluids. However, due to the high thermal conductivity of the liquid metals used, the governing heat transfer mechanisms differ fundamentally from those of conventional fluids. In this work, the heat transport mechanisms present in the TES were examined for different Péclet numbers. The analysis revealed that axial heat transport across the thermocline region is the dominant mechanism. By contrast, the heat transfer between particles and fluid, as well as the intra-particle heat conduction, contribute only marginally to the overall axial heat dispersion and, consequently, to thermocline propagation. For low Péclet numbers, where molecular heat conduction dominates, axial heat dispersion can be described for liquid metals using established correlations. For these Péclet numbers, the model developed here was successfully validated against experimental data ($Pe_0 \leq 0.32$). However, for moderate Péclet numbers, which may occur in industrial-scale TES, the effective transport parameters are subject to high uncertainties. Further research is therefore needed in this area.

1. Introduction

For the success of the energy transition, an increased use of renewable energy sources is necessary. However, since wind and solar power fluctuate significantly during the day and do not always match the demand, efficient large-scale energy storage systems are required to ensure grid stability [1]. The most important requirements for the necessary storage systems are low costs and independence of geographical requirements. For this reason, the so-called Carnot battery is of particular interest [2]. In this concept, electricity is taken from the grid during times of surplus and low cost. Then it is converted into heat using a power-to-heat cycle and stored in a thermal energy storage (TES). When electricity demand again exceeds the supply from renewable sources, the stored heat is reconverted to electricity using a heat-to-power cycle (see Fig. 1). As a core component of the Carnot battery, TES systems are therefore of particular importance. In general, a distinction is made between sensible, latent, and thermochemical storage systems. Efficiencies and exergy losses in the power-to-heat and heat-to-power cycle are not addressed in this paper as the main focus will be on sensible TES systems.

To reduce costs and increase storage capacity, single-tank systems with a packed bed have been proposed as sensible TES [3]. In this storage concept, a hot layer forms in the upper part of the storage and a cold layer forms in the lower part during charging and discharging (see Fig. 1). A transition zone develops in between, the so-called thermocline. The thickness of the thermocline indicates the exergy loss in the TES system and should therefore be as small as possible [4]. As heat transfer fluids (HTF), molten salts or thermal oils have been used so far in laboratory and pilot-scale facilities for packed-bed TES [3,5]. Molten salts are already commercially used as storage medium in two-tank TES systems [6]. A disadvantage of using thermal oils or molten

☆ This article is part of a Special issue entitled: 'ECOS2025' published in Applied Thermal Engineering.

* Corresponding authors.
E-mail addresses: eike.schmidt@kit.edu (E.A. Schmidt), klarissa.niedermeier@kit.edu (K. Niedermeier).

https://doi.org/10.1016/j.applthermaleng.2026.131680
Received 15 January 2026; Received in revised form 21 April 2026; Accepted 27 May 2026
Available online 2 June 2026

Nomenclature

Acronyms

GUM	Guide to the expression of uncertainty in measurement
HTF	heat transfer fluid
KALLA	Karlsruhe Liquid Metal Laboratory
LBE	lead-bismuth eutectic
TC	thermocouple
TES	thermal energy storage

Subscripts

0	initial
amb	ambient
bed	packed bed
exp	experimentally measured
f	fluid
i	inner
in	inlet
ins	insulation
o	outer
p	particle/solid filler material
sim	simulated
TES	thermal energy storage (liquid and packed-bed)
w	wall

Latin letters

$\Delta\overline{T}_{\mathrm{rel}}$	mean relative deviation between measured and simulated temperatures (median value derived from Monte Carlo simulation) (%)
$\Delta T_{\mathrm{rel,max}}$	maximum relative deviation between measured and simulated temperatures (median value derived from Monte Carlo simulation) (%)
ΔT_{rel}	relative deviation between measured and simulated temperatures (%)
$\dot{m}$	mass flow rate ($\mathrm{kg\,s^{-1}}$)
A	surface area ($\mathrm{m^2}$)
A_i	contribution to overall axial heat dispersion (index 1 = axial heat transport; 2 = heat transfer between particle and fluid; 3 = intra-particle heat conduction) (–)
c_{p}	heat capacity ($\mathrm{J\,kg^{-1}\,K^{-1}}$)
D	diameter of the packed bed (m)
d_{p}	particle diameter (m)
f_a	shape factor (–)
H	height of the packed bed (m)
k	overall heat transfer coefficient ($\mathrm{W\,m^{-2}\,K^{-1}}$)
r_i	relative contribution to overall axial heat dispersion (index 1 = axial heat transport; 2 = heat transfer between particles and fluid; 3 = intra-particle heat conduction) (–)
s	thickness (m)
s_{v}	specific surface area of all particles in the packed bed ($\mathrm{m^{-1}}$)
T	temperature (K)
t	time (s)
u_0	superficial fluid velocity ($\mathrm{m\,s^{-1}}$)
u_ε	interstitial fluid velocity ($\mathrm{m\,s^{-1}}$)
V	volume ($\mathrm{m^3}$)
x	storage height coordinate (m)
y	particle radius coordinate (m)

Greek letters

α	heat transfer coefficient ($\mathrm{W\,m^{-2}\,K^{-1}}$)
δ	diffusion coefficient ($\mathrm{m^2\,s^{-1}}$)
δ_{ax}	effective axial diffusion coefficient ($\mathrm{m^2\,s^{-1}}$)
λ	thermal conductivity ($\mathrm{W\,m^{-1}\,K^{-1}}$)
Λ_{ax}	effective axial thermal conductivity ($\mathrm{W\,m^{-1}\,K^{-1}}$)
μ	dynamic viscosity (Pa s)
ρ	density ($\mathrm{kg\,m^{-3}}$)
σ	standard deviation (K or %)
ε	porosity (–)

Non-dimensional parameters

Bi	Biot number: $\mathrm{Bi} = \frac{\alpha(d_{\mathrm{p}}/2)}{\lambda_{\mathrm{p}}}$
K	capacity ratio: $\mathrm{K} = \frac{(1-\varepsilon)\rho_{\mathrm{p}} c_{p,\mathrm{p}}}{\varepsilon \rho_{\mathrm{f}} c_{p,\mathrm{f}}}$
Nu	Nusselt number: $\mathrm{Nu} = \frac{\alpha d_{\mathrm{p}}}{\lambda_{\mathrm{f}}}$
Pe	Péclet number: $\mathrm{Pe}_0 = \mathrm{Re}_0\mathrm{Pr}$ or $\mathrm{Pe}_\varepsilon = \mathrm{Re}_\varepsilon\mathrm{Pr}$; $\mathrm{Pe}_0 = \mathrm{Re}_0\mathrm{Sc}$ or $\mathrm{Pe}_\varepsilon = \mathrm{Re}_\varepsilon\mathrm{Sc}$
$\mathrm{Pe}_{\mathrm{ax}}$	effective axial Péclet number: $\mathrm{Pe}_{\mathrm{ax}} = \frac{d_{\mathrm{p}} u_0 \rho_{\mathrm{f}} c_{p,\mathrm{f}}}{\Lambda_{\mathrm{ax}}}$ or $\mathrm{Pe}_{\mathrm{ax}} = \frac{d_{\mathrm{p}} u_0}{\delta_{\mathrm{ax}}}$
Pr	Prandtl number: $\mathrm{Pr} = \frac{\mu_{\mathrm{f}} c_{p,\mathrm{f}}}{\lambda_{\mathrm{f}}}$
Re	Reynolds number: $\mathrm{Re}_0 = \frac{\rho_{\mathrm{f}} u_0 d_{\mathrm{p}}}{\mu_{\mathrm{f}}}$ or $\mathrm{Re}_\varepsilon = \frac{\rho_{\mathrm{f}} u_\varepsilon d_{\mathrm{p}}}{\mu_{\mathrm{f}}}$
Sc	Schmidt number: $\mathrm{Sc} = \frac{\mu_{\mathrm{f}}}{\rho_{\mathrm{f}} \delta}$

salts is their relatively low thermal conductivity, which leads to only moderate heat transfer [7]. As an alternative HTF in packed-bed TES, liquid metals have been proposed [8–10]. A detailed overview of TES experiments using liquid metals as HTF is given by Niedermeier [11]. In contrast to conventional fluids, their thermal conductivity is up to 100 times higher, enabling efficient heat transfer [12]. Furthermore, liquid metals remain stable over a wide temperature range, allowing large temperature differences inside the TES. For example, the liquid range of sodium is 98 °C to 883 °C, and the liquid range of lead is 327 °C to 1743 °C [13]. Consequently, high storage capacities can be achieved [7] and high-temperature applications well above 500 °C are possible [11].

1.1. Previous work at Karlsruhe Liquid Metal Laboratory on TES and novelty of this paper

At the Karlsruhe Liquid Metal Laboratory (KALLA), packed-bed TES systems are currently being investigated, in which liquid metals are used as HTF. Based on simulations using a heterogeneous continuum model with a dispersed solid phase, competitiveness with other packed-bed TES systems with molten salts as HTF has been demonstrated [15]. The storage concept was also successfully tested in a lab-scale experiment by Müller-Trefzer et al. [16]. For this purpose, a TES unit with a thermal capacity of approximately 1 kWh was constructed. Zirconium silicate spheres with a diameter of about 2.65 mm were used as the filler material. The monodisperse packing enabled a porosity of approximately 36 %. Because of the existing infrastructure at KALLA, lead-bismuth eutectic (LBE) was used as a model HTF with a Prandtl number of around 0.03. Considering the constraints of the test loop and

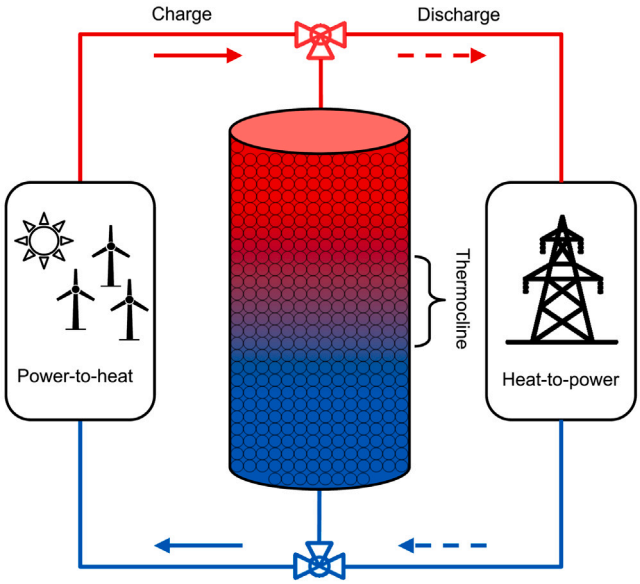

Fig. 1. Schematic representation of a packed-bed TES system as part of a Carnot battery.
Source: Adapted from [14]

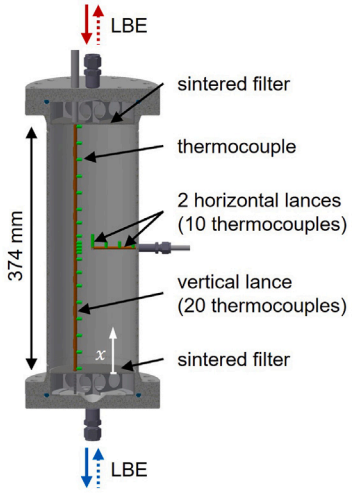

Fig. 2. CAD drawing of the lab-scale experiment (compare [16]; CAD-Drawing: KIT/Daubner). The TES is filled with zirconium silicate spheres with a diameter of approximately 2.65 mm and a bed porosity of approximately 36 %.

the fluid properties, storage temperatures between 180 °C and 380 °C could be realized. The temperatures during the experiment were measured using a total of 30 thermocouples, which were distributed along a vertical "thermocouple lance" and two centrally placed horizontal "thermocouple lances" (see Fig. 2). In the experiment, Péclet numbers ($Pe_0 = Re_0 \cdot Pr$) between 0.06 and 0.32 were achieved, corresponding to an interstitial fluid velocity between 0.4 and 2.3 mm s^{-1}. For more information on the experimental data used in this study, the interested reader is referred to [17].

Based on the findings from the lab-scale experiment, a 100 kWh pilot-scale TES is currently under construction. LBE serves again as model HTF, and zirconium silicate spheres are again being used as filler material. In contrast to the lab-scale experiment, higher flow velocities and thus discharge powers can be realized in the pilot-scale TES, which might be relevant for industrial-scale application. The experiment's limited maximum temperature of 450 °C does not limit its relevance for high temperature TES based on liquid metals, as the heat transfer processes are primarily governed by temperature differences rather than the absolute temperature level. Only temperature-dependent material properties and losses to the environment could be affected: the former is addressed by using non-dimensional representations for the evaluation of results, and the latter is minimized in any case by insulation measures. The pronounced corrosiveness of liquid metals at higher temperature levels is a major challenge in later industrial application, necessitating research into suitable filler materials [18,19] and the operability of components such as pumps and valves [20].

Although the numerical model developed by Niedermeier et al. [15] for simulating the thermocline propagation was successfully validated using literature data from TES systems with thermal oil and molten salt, it did not adequately capture the behavior observed in a lab-scale experiment. Deviations of up to 20 K between simulated and measured temperatures were reported [16]. Apparently, the heat transport phenomena of liquid metals and the boundary conditions of the lab-scale experiment could not be sufficiently modeled with the assumptions and simplifications made. However, the accurate simulation and modeling of TES systems is essential for both optimization and targeted design. In particular, the calculation of the thermocline propagation during charging and discharging in single-tank configurations plays an important role. This study therefore aims to investigate the underlying heat transport phenomena for liquid metals in more detail and to extend the numerical model of the TES so that validation with the experimental data from the lab-scale experiment becomes possible. Furthermore, the influence of the Péclet number on the modeling of the TES system will be examined. This will allow conclusions about the modeling of the pilot-scale TES and highlight existing knowledge gaps in the modeling of heat transport in packed beds with liquid metal flow.

1.2. Simulation of packed-bed TES systems

TES systems can reach large dimensions and as a consequence high-resolution CFD simulations are typically not performed. Especially when a packed bed is present in the TES, the required computational effort would be too high for most applications. Instead, continuum models are often used. Rather than resolving all pores individually, these models are averaged over larger volume elements [21]. Since local transport phenomena are not resolved, effective transport coefficients for heat transport phenomena are required for the modeling process [22].

Depending on the required level of detail, the models are formulated as one- or two-dimensional. Furthermore, a distinction is made between homogeneous and heterogeneous models. In homogeneous models, the temperature difference between the fluid and the particles is neglected, and the fluid and solid are treated as a single continuous phase [23]. In heterogeneous models, however, the two phases are considered separately. In this case, either both the fluid and solid phases are modeled as continuous phases, or the solid phase is represented as a dispersed phase. A disadvantage of the continuous solid phase approach is that separate effective transport parameters are required to describe axial heat transport in both the solid and fluid phases [24]. However, these two phenomena are difficult to separate. In contrast, modeling the solid phase as a dispersed phase offers the advantage that only one effective thermal conductivity is needed. This value is included in the differential equation of the fluid phase but also accounts for the influence of the packed bed [24]. To capture thermal conductivity within the spherical particles, a temperature field with concentric isotherms is assumed and calculated within the particles [24]. Heat transfer in a packed bed subject to flow of conventional fluids has been extensively investigated in the past [24,25]. The center of a temperature marker moves through an infinitely extended packed bed by advection. The velocity of the

advective propagation is solely influenced by the interstitial fluid velocity and the capacity ratio K between the solid and the liquid phases (Eq. (1)) taking the bed porosity ε into account [25].

$$K = \frac{(1-\varepsilon)\rho_{\mathrm{p}} c_{p,\mathrm{p}}}{\varepsilon \rho_{\mathrm{f}} c_{p,\mathrm{f}}} \tag{1}$$

However, for the diffusive propagation of a temperature marker, and thus the broadening of the thermocline region in a packed-bed TES, three mechanisms have been identified that are responsible for axial heat dispersion: axial heat transport, heat transfer between fluid and particles, and intra-particle heat conduction [25]. Axial heat transport is due to molecular heat conduction in both the solid and fluid phases, as well as heat transport caused by turbulent mixing, with both mechanisms acting across the thermocline (i.e. along the vertical axis of the packed bed) (see also Section 2.2).

From the derivation of a transfer function for a heterogeneous continuum model with dispersed solid phase, Tsotsas [25] obtained the Eqs. (2)–(5), which enable the calculation of the relative contributions r_i of the three heat transport mechanisms to the overall axial heat dispersion. For detailed derivation, the authors refer to the original literature [25]. Hereby, index 1 refers to the contribution of axial heat transport, 2 to the heat transfer between particles and fluid, and 3 to the contribution of intra-particle heat conduction. The axial heat transport is mainly described by the effective thermal conductivity Λ_{ax} and the heat transfer between particles and fluid by the Nusselt number Nu.

$$r_i = \frac{A_i}{\sum_{i=1}^{3} A_i}, \tag{2}$$

with

$$A_1 = \frac{(1+K)^2}{\mathrm{Pe}_0} \cdot \frac{\Lambda_{\mathrm{ax}}}{\lambda_{\mathrm{f}}}, \tag{3}$$

$$A_2 = \frac{K^2 \cdot \mathrm{Pe}_0}{6(1-\varepsilon)\mathrm{Nu}}, \tag{4}$$

$$A_3 = \frac{K^2 \cdot \mathrm{Pe}_0}{60(1-\varepsilon) \cdot \lambda_{\mathrm{p}}/\lambda_{\mathrm{f}}}. \tag{5}$$

As an important simplification for this analytical approach, the temperature dependence of material properties and the influence of the tank wall are neglected [25].

The influence of individual heat transport mechanisms on the overall axial heat dispersion strongly depends on the Péclet number. Based on a preliminary assessment of the dominant mechanisms for the Péclet number range under investigation, the necessary effective transport parameters can be determined. This ensures that the relevant heat transport mechanisms are taken into account in the simulation.

2. Heat transport mechanisms in packed beds with liquid metal flow

Because of the high thermal conductivity and comparatively low viscosity of liquid metals, several particularities arise in comparison to conventional fluids. The thermal boundary layer is significantly thicker than the hydrodynamic boundary layer, which is expressed by the characteristically low Prandtl number of liquid metals. Consequently, heat transfer in a turbulent bulk flow is strongly influenced by molecular heat conduction [26]. Due to this fundamental difference in heat transfer, correlations derived for conventional fluids cannot be applied to turbulent liquid metal flow [26]. With the exception of intra-particle heat conduction, which is independent of the HTF used, this has a major impact on the calculation of the heat transport mechanisms mentioned in Section 1.2. The following provides an overview of the existing knowledge on relevant heat transfer mechanisms and identifies existing research gaps. Furthermore, conclusions will be drawn regarding the implications of simulating packed-bed TES systems using liquid metals as HTF.

2.1. Heat transfer between fluid and particles and between fluid and wall

To the best of the authors' knowledge, there are no valid correlations for the heat transfer between fluid and particles in a packed bed with a liquid metal flow. However, Melissari and Argyropoulos [27] experimentally determined a correlation for forced liquid metal convection around a single sphere (Eq. (6)):

$$\mathrm{Nu} = 2 + 0.47 \cdot \mathrm{Re}_{\varepsilon}^{1/2} \cdot \mathrm{Pr}^{0.36} \tag{6}$$

Ahmed and Yovanovich [28] analytically derived an equation for a single sphere in cross-flow applicable to all Prandtl numbers. The calculated Nusselt numbers agree with those from Eq. (6) within a deviation of less than 1 %, for the relevant Prandtl number in this study of approximately 0.03.

Since the Nusselt number of a packed bed is always greater than that of a single sphere [29], a minimum Nusselt number for a packed bed through which liquid metal flows can be estimated. For heat transfer between fluid and wall, several correlations exist for pipe flows under various boundary conditions [30,31]. However, to the best of the authors' knowledge, no correlations have been validated for liquid metals with a packed bed.

2.2. Axial heat transport

As mentioned above, continuum models do not resolve each individual particle but instead average over larger volumes. Axial heat transport is described in this context by the effective thermal conductivity [24,25]. The effective thermal conductivity accounts for molecular heat conduction in both the solid and fluid phases, as well as heat transport due to turbulent mixing. This leads to an asymptotic behavior for very low and very high Péclet numbers (see Fig. 3). At low Péclet numbers, molecular heat conduction dominates, and the effective thermal conductivity approaches the conductivity of the packed bed under stagnant conditions λ_{bed}. This limiting value can be calculated with the model by Zehner, Bauer, and Schlünder [32], which has been validated for the $\lambda_{\mathrm{p}}/\lambda_{\mathrm{f}}$ ratio relevant to liquid metals. Since the correlation refers to a stagnant fluid and purely molecular heat conduction, no differences in behavior between liquid metals and conventional fluids are to be expected. In contrast, at very high Péclet numbers, heat transport is governed solely by turbulent mixing of the fluid. In this case, a theoretical limiting value for axial heat transport can be derived from a cascade of ideally mixed reactors [33]. For the transition region between these two limits, Tsotsas [22] and Wakao and Kaguei [24] recommend Eq. (7) for calculating the effective thermal conductivity Λ_{ax}.

$$\Lambda_{\mathrm{ax}} = \lambda_{\mathrm{bed}} + 0.5\mathrm{Pe}_0 \lambda_{\mathrm{f}} \tag{7}$$

However, only few studies exist, in which the Prandtl number is varied. Experiments were often conducted with gases, which usually have a Prandtl number of approximately 0.7 [25]. The Prandtl number for liquid metals, however, is typically an order of magnitude lower (e.g., for LBE at 250 °C, Pr ≈ 0.03 [26]). In addition, the fundamental differences in the heat transport mechanisms between liquid metals and conventional fluids described above must be considered. Therefore, based on the current state of knowledge, the effective thermal conductivity of packed beds with liquid metal flow cannot be reliably determined in the transition region between the two asymptotic limits. Fig. 3 shows that the pilot-scale TES system currently under construction at KALLA operates in this transition region. In contrast, due to the significantly lower flow velocity in the lab-scale experiment, its Péclet number range is largely outside the transition region, where no significant deviation from Eq. (7) is expected.

In addition to the specific characteristics of low-Prandtl-number fluids, it should be noted that a dependence of the effective axial Péclet number $\mathrm{Pe}_{\mathrm{ax}}$ on the Schmidt number ($\mathrm{Sc} = \mu_{\mathrm{f}}/(\rho_{\mathrm{f}}\,\delta)$) has been observed in a large number of mass transport experiments. The analogy between heat and mass transfer permits the transfer of insights from

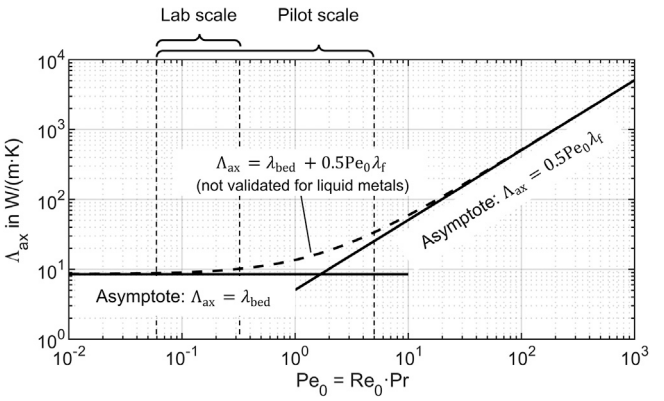

Fig. 3. Asymptotic behavior of the effective thermal conductivity for LBE (Pr ≈ 0.03) and a packed bed of zirconium silicate spheres (d_p = 2.65 mm, ε = 36 %). Furthermore, the Péclet number range of the lab- and pilot-scale experiments at KALLA are depicted.

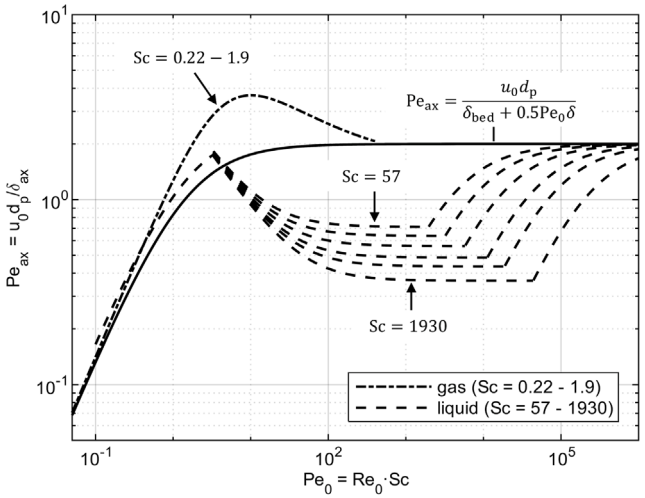

Fig. 4. Effective axial Péclet number Pe_{ax} for different Schmidt numbers (compare [34]). The reference value for the axial Péclet number (solid line) is calculated with Eq. (9) for the effective diffusion coefficient δ_{ax}.

mass transport experiments to heat transfer phenomena. The Schmidt and Prandtl numbers are interchangeable in the corresponding correlations. Consequently, the effective axial Péclet number Pe_{ax} can be defined with the effective axial thermal conductivity for heat transport or with the effective axial diffusion coefficient for mass transport respectively (Eq. (8)).

$$Pe_{ax} = \frac{d_p u_0 \rho_f c_{p,f}}{\Lambda_{ax}} \text{ or } Pe_{ax} = \frac{d_p u_0}{\delta_{ax}} \tag{8}$$

Through the analysis of a large number of mass-transport experiments, Delgado [34] was able to fit empirical correlations that allow the calculation of the effective axial Péclet number for various Schmidt numbers. A distinction is made between gases, which typically have low Schmidt numbers, and liquids, which exhibit substantially higher Schmidt numbers. As shown in Fig. 4, both liquids and gases exhibit a pronounced deviation in the actual evolution of Pe_{ax} from the reference value. This reference value is calculated using the effective axial diffusion coefficient δ_{ax} according to Eq. (9) (see also the analogous Eq. (7) for heat transport) [22].

$$\delta_{ax} = \delta_{bed} + 0.5\,Pe_0\,\delta \tag{9}$$

In the transition region at moderate Péclet numbers, gases are observed to attain higher Pe_{ax} values in the experiments than predicted using Eq. (9). In contrast, for liquids, Pe_{ax} decreases with increasing Schmidt number in the transition region. The observed Schmidt number dependency is likely caused by a combination of microscopic flow maldistribution and radial molecular diffusion [22,35].

Since the lowest Schmidt number examined in the mass transport experiments (Sc = 0.2) is an order of magnitude higher than the Prandtl number of liquid metals (for LBE, Pr ≈ 0.03), the empirical correlations derived by Delgado [34] cannot be transferred to liquid metals using the analogy between heat and mass transfer. However, the observations reinforce the hypothesis that deviations from Eq. (7) in the transition regime at moderate Péclet numbers are expected for the effective thermal conductivity of a liquid-metal flow in a packed bed due to its low Prandtl number.

2.3. Relative contributions of individual heat transport mechanisms to the overall axial heat dispersion for TES with liquid metal

Based on the method described in Section 1.2, the relative contributions of the heat transport mechanisms to the axial heat dispersion are analyzed. The results for an exemplary TES based on the storage concept investigated at KALLA are presented in Fig. 5. Similar to

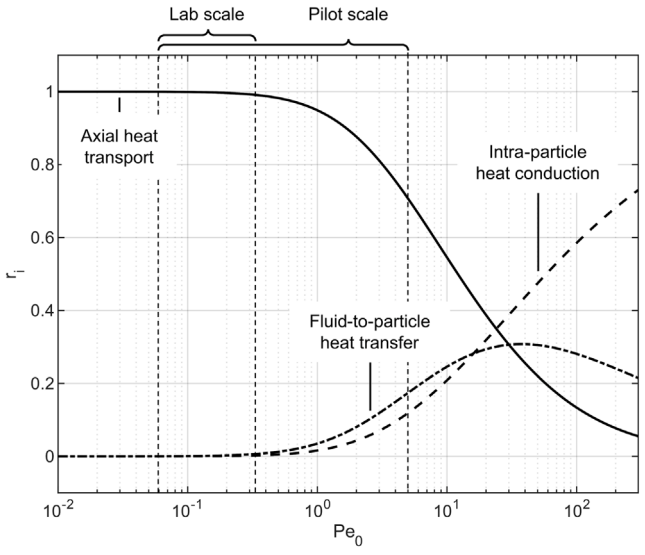

Fig. 5. Relative contributions of the heat transport mechanisms to the overall axial heat dispersion for LBE (Pr ≈ 0.03) and a packed bed of zirconium silicate spheres (d_p = 2.65 mm, ε = 36 %). Furthermore, the Péclet number range of the lab- and pilot-scale experiments at KALLA are depicted.

the lab-scale experiment and the pilot-scale TES currently under construction, zirconium silicate spheres with a diameter of approximately 2.65 mm are used and a porosity of 36 % is assumed. As HTF, LBE at a temperature of 280 °C is selected. Due to the lack of a validated equation, the heat transfer between fluid and particles is calculated using the correlation by Ahmed and Yovanovich [28]. In comparison to the correlation by Melissari and Argyropoulos [27] (Eq. (6)), this correlation has the advantage that its range of validity is not limited for low Reynolds numbers and therefore a continuous calculation is possible. For the effective thermal conductivity, the recommended correlation for conventional fluids (Eq. (7)) is used. As shown in Section 2.2, this correlation is subject to considerable uncertainties for low Prandtl number fluids. As a consequence, the following analysis can only be used to identify trends. Detailed conclusions about the relative contributions of the heat transport mechanisms are therefore not possible.

As shown in Fig. 5, at very low Péclet numbers, axial heat transport dominates. With increasing Péclet number, the contribution of axial heat transport decreases, and intra-particle heat conduction as well as heat transfer between particles and fluid become more significant. While heat transfer between particles and fluid may reach a maximum at moderate Péclet numbers, intra-particle heat conduction dominates at very high Péclet numbers. It is noticeable that the curve describing the relative contribution of the heat transfer between fluid and particles shows a relatively low peak. Due to the high thermal conductivity of liquid metals, heat transfer between particles and fluid might not dominating at any Péclet number.

Additionally, the operating range of the pilot-scale TES and the lab-scale experiment is indicated in Fig. 5. Both in the lab-scale experiment and in the pilot-scale TES, axial heat transport is most likely the dominant mechanism. In the lab-scale experiment, heat transfer between particles and fluid as well as intra-particle heat conduction have a negligibly small influence on axial heat dispersion. In contrast, at moderate to high Péclet numbers in the pilot-scale TES, the influence of these two mechanisms seems to be non-negligible. This is different for conventional fluids. Here, heat transfer between particles and fluid clearly dominates over a wide Péclet-number range.

2.4. Conclusion for the simulation of TES with liquid metal as HTF

As shown in Section 2.2, the effective thermal conductivity in the Péclet number range relevant to the lab-scale experiment is primarily governed by molecular heat conduction. Therefore, it can be assumed that the lab-scale experiment can be well simulated with known correlations. In contrast, the simulation of the pilot-scale TES must account for uncertainties in both the determination of the heat transfer coefficient and the effective thermal conductivity. Consequently, in the following, a distinction is made between simulations at low Péclet numbers (Section 4), where axial heat dispersion is dominated by molecular heat conduction, and simulations at moderate Péclet numbers (Section 5), where additional mechanisms contribute significantly to the overall heat dispersion. Since intra-particle heat conduction dominates at very high Péclet numbers, no particular phenomena are expected from the use of liquid metals as HTF in this regime. Moreover, due to the necessarily high pumping power and unrealistically short discharge times, this regime lies outside the operating range of the TES systems. For this reason, high Péclet numbers will not be considered further in the following.

3. Formulation and extension of the numerical model

Based on the investigation of the heat transport phenomena described in Section 2 and a sensitivity analysis of the parameters used, the numerical model published by Niedermeier et al. [15] was extended and is in the following referred to as the "extended model". The basis is a one-dimensional heterogeneous continuum model with a dispersed solid phase. In the original model, it was simplistically assumed that heat transport occurs only in the liquid phase and can therefore be described by the product of porosity and the thermal conductivity of the fluid. In contrast, the extended model uses the effective thermal conductivity presented in Section 2.2. Since liquid metals are opaque, the radiative contribution to the thermal transport is neglected in the calculation, as in the entire rest of the model. To calculate the heat transfer coefficient between fluid and particles, the correlation for a single sphere with convective flow (Eq. (6)) is used. If the Péclet number falls below the valid range of the correlation ($1 \times 10^2 \leq \mathrm{Re}_\varepsilon \leq 5 \times 10^4$) [27] due to very low flow velocity, a simplified assumption of the minimum possible Nusselt number of Nu = 2 for a sphere in cross flow is made.

A sensitivity analysis of the material properties revealed that the temperature dependence of the fluid's thermal conductivity as well as the heat capacities should not be neglected and it is therefore included in the extended model.

In the lab-scale experiment, the tank wall accounted for approximately 19 % of the total heat capacity of the TES system. Therefore, the influence of the wall's heat capacity cannot be neglected. To account for this, the numerical model is extended by an energy balance for the wall. Due to the lack of a validated correlation for the heat transfer coefficient between the wall and the fluid for liquid metals, an ideal heat transfer is assumed at this point ($T_\mathrm{f} \approx T_\mathrm{w}$). Due to the small cross-sectional area of the wall compared to the packed bed and the similar thermal conductivity of the stainless steel used compared to that of the liquid metal, an additional axial path through the wall is neglected.

Especially in simulations of long-duration charging and discharging processes, it is also important to account for heat loss to the ambient. This can be approximated in a quasi-steady manner using an overall heat transfer coefficient k that considers the various insulation layers of the TES system and the heat transfer from the surface of the insulation to the surroundings α (Eq. (10)).

$$\frac{1}{kA} = \frac{1}{\alpha A} + \sum_j \left(\frac{s_\mathrm{ins}}{\lambda_\mathrm{ins} \cdot \frac{A_\mathrm{o} - A_\mathrm{i}}{\ln\left(\frac{A_\mathrm{o}}{A_\mathrm{i}}\right)}} \right)_j \tag{10}$$

From the extensions described above, the energy equation system Eq. (11)–(13) results. Eq. (11) describes the energy balance of the fluid and accounts for both advection and diffusion of heat along the axial coordinate x. Heat conduction on the single-particle scale is represented by Eq. (12), where y denotes the particle-radius coordinate. Eq. (13) gives the energy balance of the wall and accounts for heat loss to the surrounding environment. The three equations are coupled through the heat transfer coefficient between fluid and particle α_p and the heat transfer coefficient between fluid and wall α_w.

$$\varepsilon \rho_\mathrm{f} c_{p,\mathrm{f}}(T_\mathrm{f}) \left(\frac{\partial T_\mathrm{f}}{\partial t} + u_\varepsilon \frac{\partial T_\mathrm{f}}{\partial x} \right) = \frac{\partial}{\partial x} \left(\Lambda_\mathrm{ax}(T_\mathrm{f}) \frac{\partial T_\mathrm{f}}{\partial x} \right) - \alpha_\mathrm{p} s_\mathrm{v} \left(T_\mathrm{f} - T_{\mathrm{p},\, y=d_\mathrm{p}/2} \right) - \frac{\alpha_\mathrm{w} A_\mathrm{w}}{V_\mathrm{TES}} \left(T_\mathrm{f} - T_\mathrm{w} \right) \tag{11}$$

$$\rho_\mathrm{p} c_{p,\mathrm{p}}(T_\mathrm{p}) \frac{\partial T_\mathrm{p}}{\partial t} = \lambda_\mathrm{p} \left(\frac{\partial^2 T_\mathrm{p}}{\partial y^2} + \frac{2}{y} \frac{\partial T_\mathrm{p}}{\partial y} \right) \tag{12}$$

$$\rho_\mathrm{w} V_\mathrm{w} c_{p,\mathrm{w}}(T_\mathrm{w}) \frac{\partial T_\mathrm{w}}{\partial t} = \alpha_\mathrm{w} A_\mathrm{w} \left(T_\mathrm{f} - T_\mathrm{w} \right) - kA \left(T_\mathrm{w} - T_\mathrm{amb} \right) \tag{13}$$

Here, s_v denotes the specific surface area of all particles in the packed bed and can be calculated according to Eq. (14).

$$s_\mathrm{v} = \frac{6(1-\varepsilon)}{d_\mathrm{p}} \tag{14}$$

At low Péclet numbers, when intra-particle heat conduction is not limiting, the temperature gradient within the particles can be neglected. In this case, Eq. (12) is replaced by Eq. (15).

$$(1-\varepsilon) \rho_\mathrm{p} c_{p,\mathrm{p}}(T_\mathrm{p}) \frac{\partial T_\mathrm{p}}{\partial t} = \alpha_\mathrm{p} s_\mathrm{v} \left(T_\mathrm{f} - T_\mathrm{p} \right). \tag{15}$$

This simplification offers the advantage of significantly reducing computational effort. However, according to the current state of the art, the maximum Péclet number for which this simplification remains valid for low Prandtl number fluids can only be estimated (compare Fig. 5), and verification of this assumption is required in each specific case.

3.1. Approach for numerical solution and boundary and initial conditions

The differential equations are discretized in time using the Crank-Nicholson method and solved in MATLAB®. For the advective term, a first-order upwind difference scheme and for the diffusive term a central difference scheme is applied. To ensure adequate differentiation, a grid sensitivity study was conducted. The initial condition specifies the temperatures of the fluid, the particles, and the wall at the beginning of

the simulation (Eq. (16)). A Dirichlet boundary condition is applied at the inlet (Eq. (17)), and a zero heat flux boundary condition is assumed at the outlet (Eq. (18)).

$$T_f(t=0) = T_p(t=0) = T_w(t=0) = T_0 \tag{16}$$

$$T_f(x=0) = T_{in} \tag{17}$$

$$\left.\frac{\partial T_f}{\partial x}\right|_{x=H} = 0 \tag{18}$$

If the temperature gradient within the particle is to be considered using Eq. (12), a zero heat flux boundary condition is also assumed at the center of the particle due to symmetry (Eq. (19)). At the particle surface, convective heat transfer occurs (Eq. (20)).

$$\left.\frac{\partial T_p}{\partial y}\right|_{y=0} = 0 \tag{19}$$

$$\lambda_p \left.\frac{\partial T_p}{\partial y}\right|_{y=\frac{d_p}{2}} = \alpha_p \left(T_f - T_p\big|_{y=\frac{d_p}{2}}\right) \tag{20}$$

4. Simulation of the lab-scale storage experiment with liquid metal as HTF at low Péclet numbers

The numerical model established in Section 3 is to be validated for low Péclet numbers using the experimental data of the lab-scale experiment [17] described in Section 1.1 and which have been evaluated by Müller-Trefzer et al. [16]. Because of the low Péclet number, the temperature gradient within the particles is neglected and Eq. (15) is applied. The validity of this simplification is discussed in Section 4.3.4.

The insulation of the lab-scale experiment consisted of a single layer of mineral wool. Since the temperature was measured at the surface of the insulation, the ambient temperature T_{amb} in Eq. (13) can be replaced by the surface temperature T_{ins}. Accordingly, the term for heat transfer to the surroundings is omitted in the calculation of the overall heat transfer coefficient (Eq. (10)). The surface temperature of the insulation was measured at only one single location. Therefore, a homogeneous temperature distribution on the surface of the insulation is assumed.

Due to the specific design of the test section, a sharp temperature step could not be realized. The fluid initially interacted with the inlet and outlet flanges, whose high thermal capacity had a considerable impact on the initial temperature profile [16]. Therefore, the measured temperature at the first thermocouple of the vertical thermocouple lance (see Fig. 2) is used as the inlet temperature for the simulation. This places the flanges outside the energy balance and thus, they do not need to be considered in the simulation. The initial condition for the simulation was defined using the measured temperatures along the vertical thermocouple lance at the beginning of the experiment, whereby the radial temperature distribution is assumed to be negligible.

During the experiments, the mass flow rate was measured. Based on Eq. (21), the superficial fluid velocity can thus be determined, which in turn allows the calculation of the Péclet number for the respective experiment.

$$u_0 = \frac{4\dot{m}}{\rho_f \pi D^2} \tag{21}$$

Overall, eleven charging and seventeen discharging experiments at different temperature levels and Péclet numbers between $Pe_0 \approx 0.06 - 0.32$ were evaluated. In the experiments, the TES was charged and discharged up to half of its total thermal capacity [16,17], so that the temperature profile along the vertical axis of the storage could be analyzed. The material properties and geometric parameters used are listed in Table 1.

4.1. Uncertainty analysis with Monte Carlo method

A large number of thermophysical properties and measured initial and inlet conditions are incorporated into the simulation. These are naturally subject to uncertainties, which affect the simulation results. To account for these uncertainties, Monte Carlo simulations were therefore carried out. For this purpose, a probability distribution is assigned to each input parameter, and the simulation is executed thousands of times using statistically varied values. In this case, approximately 20 000 repetitions have proven to be sufficient, as halving the number of simulations only altered the second decimal place. From this, the 95 % confidence interval of the storage simulation can be determined.

The material data and measured parameters used, along with their respective uncertainties, are shown in Table 1. Since no specific probability distribution of uncertainties is known for most parameters, a uniform distribution is assumed. The measurement uncertainty of the calibrated thermocouples have been determined based on the “Guide to the expression of uncertainty in measurement” (GUM) [36] and assumed to be normally distributed [17]. The mass flow rate was obtained in the experiment from a differential pressure measurement in the supply tank [16]. Both the measurement uncertainties and the uncertainties associated with determining the regression curve were evaluated with the method described by Matus [37], which is also based on the GUM [17].

Due to the lack of reliable measurement data, the uncertainties resulting from the assumption of a homogeneous temperature profile in the radial direction, as well as the assumption of a homogeneous temperature distribution at the surface of the insulation, cannot be considered in the Monte Carlo simulation.

4.2. Comparison of simulation with experimental data

The simulated temperature profiles are compared with the measured temperatures along the vertical thermocouple lance (see Fig. 2) at different time points. The relative deviation between experiment and simulation can be calculated with Eq. (22).

$$\Delta T_{rel} = \frac{T_{exp} - T_{sim}}{T_{exp}^{max} - T_{exp}^{min}} \tag{22}$$

Each experiment is simulated thousands of times using the Monte Carlo approach outlined in Section 4.1. For each simulation, the mean and maximum relative deviations are determined once the TES is half-charged or half-discharged, which was when the end of the charging/discharging experiment has been reached [16]. The values presented in the following are the medians derived from the set of simulations for each specific experiment, with the corresponding 95 % confidence interval limits shown in parentheses.

In Fig. 6, the temperature profiles for various points in time are shown exemplarily for a discharge experiment with a Péclet number of $Pe_0 \approx 0.31$ (experiment D08, see Table 2). At the end of the experiment (after 631 s), the maximum relative deviation between the measured and simulated values is approximately 3.7 % (−1.7 % to 8.2 %), and the mean deviation is less than 2.3 % (−0.3 % to 4.9 %). As shown in Fig. 6, nearly all measured values lie within the 95 % confidence interval. Only six of the plotted data points lie slightly outside the 95 % confidence interval.

The corresponding charging experiment of the TES conducted at the same Péclet number (experiment C05) is shown in Fig. 7. In contrast to the discharge experiment, most of the measured values here lie outside the 95 % confidence interval. The mean relative deviation at the end of the experiment (after 596 s) is slightly larger in absolute terms, amounting to −4.9 % (−7.5 % to −2.2 %). The higher deviation between simulation and measured values in charging experiments compared to discharging experiments can also be observed in all other investigated

Table 1
Thermophysical properties and input parameters used in the simulation, including their respective uncertainties. Values marked with * are estimates based on commonly observed uncertainties in the determination of the respective quantities.

Parameter	Value	Uncertainty	Reference
ρ_p	4224 kg m^{-3}	±5 %	[18]
$c_{p,p}$	$(-8 \cdot 10^{-4} \cdot T_p^2 + 1.1537 \cdot T_p + 331.42)$ J kg^{-1} K^{-1}	±3 %	[18]
λ_p	7.7 W m^{-1} K^{-1}	±10 %*	[18]
ρ_f	$(11065 - 1.293 \cdot T_f)$ kg m^{-3}	±0.8 %	[26]
$c_{p,f}$	$(164.8 - 3.94 \cdot 10^{-2} \cdot T_f + 1.25 \cdot 10^{-5} \cdot T_f^2 - 4.56 \cdot 10^5 \cdot T_f^{-2})$ J kg^{-1} K^{-1}	±2 %	[26]
λ_f	$(3.284 + 1.617 \cdot 10^{-2} \cdot T_f - 2.305 \cdot 10^{-6} \cdot T_f^2)$ W m^{-1} K^{-1}	±15 %	[26]
ρ_w	7980 kg m^{-3}	±0.1 %*	[38]
$c_{p,w}$	100 °C: 487 J kg^{-1} K^{-1} 200 °C: 503 J kg^{-1} K^{-1} 300 °C: 511 J kg^{-1} K^{-1} 400 °C: 520 J kg^{-1} K^{-1}	±3 %*	[39]
λ_{ins}	50 °C: 0.039 W m^{-1} K^{-1} 100 °C: 0.045 W m^{-1} K^{-1} 200 °C: 0.062 W m^{-1} K^{-1} 300 °C: 0.084 W m^{-1} K^{-1} 400 °C: 0.113 W m^{-1} K^{-1}	±10 %*	[40]
λ_{bed}	Calculated according to the model by Zehner, Bauer and Schlünder	±30 %	[32]
T_0	Measured by vertical thermocouple lance	σ = 0.35 K	[17]
T_{in}	Measured by thermocouple	σ = 0.35 K	[17]
T_{ins}	Measured by thermocouple	σ = 0.35 K	[17]
$\dot{m}$	Measured by the change of the level in the hot liquid metal reservoir	σ = 1.85 %	[16,17]
d_p	2.65 mm	±0.15 mm	[16,17]
s_w	3.5 mm	±0.1 mm*	[16,17]
s_{ins}	150 mm	±6 %*	[17]
D	130 mm	±0.1 mm*	[16,17]

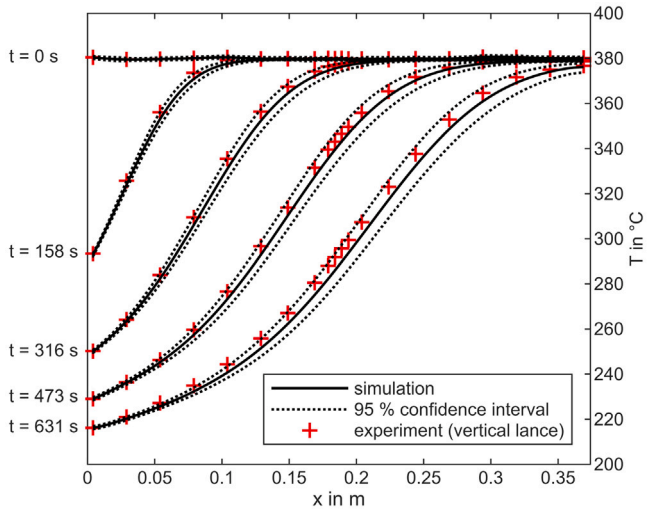

Fig. 6. Simulated temperature profiles and measured temperature values of experiment D08 at various points in time, including the respective 95 % confidence interval of the simulation. The uncertainties of the temperature measurement are very small (compare Table 1). For the sake of clarity, error bars of the measured temperature values are therefore not shown. The temperature profile at $t = 0$ s was interpolated from the measured values and used as the initial condition.

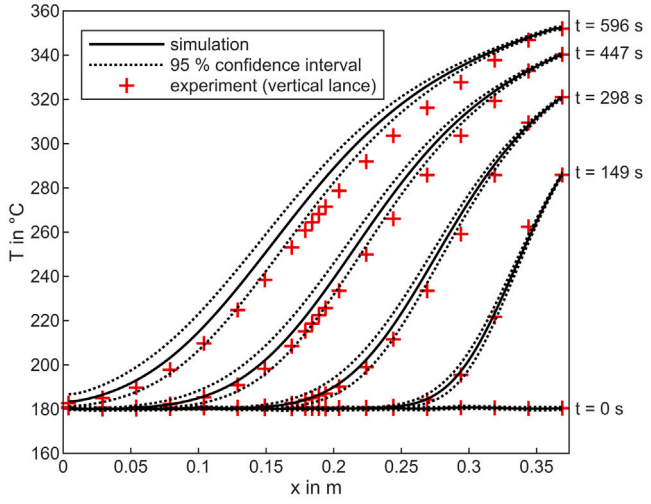

Fig. 7. Simulated temperature profiles and measured temperature values of experiment C05 at various points in time, including the respective 95 % confidence interval of the simulation. The uncertainties of the temperature measurement are very small (compare Table 1). For the sake of clarity, error bars of the measured temperature values are therefore not shown. The temperature profile at $t = 0$ s was interpolated from the measured values and used as the initial condition.

experiments (see Table 2). While the mean deviation at the end of the experiment ranges between 1.2 % and 3.6 % for discharging experiments, it ranges between −4.3 % and −8.6 % for charging experiments.

For charging experiments, a dependency of the relative deviation on the temperature level of the experiments can be observed. In experiments with a temperature level between 200 °C and 270 °C, the mean relative deviation at the end of the experiment at the same flow velocity is consistently larger in absolute terms than the mean deviations at a temperature level between 180 °C and 380 °C.

Furthermore, in experiments with a temperature level between 200 °C and 270 °C, a clear dependency of the mean relative deviation on the Péclet number can be observed. The Pearson coefficient, a linear correlation coefficient, is −0.99 and 0.99 for charging and discharging experiments respectively, indicating that the absolute value of the relative deviation becomes larger as the Péclet number increases. For charging experiments with a higher temperature difference (180 °C–380 °C), the Pearson correlation coefficient decreases to 0.6. In contrast, for discharging experiments with a temperature difference between 180 °C and 380 °C, no pronounced dependency can be observed. The Pearson coefficient is approximately −0.09.

Table 2
Operating parameters of the investigated experiments as well as the mean and maximum relative deviation between the simulated and experimentally measured values at the end of the experiment. The median value of the Monte Carlo simulation is given in each case, along with the bounds of the 95 % confidence interval in parentheses.

ID	Mode	Temperature range	Pe_0	$\Delta\overline{T}_{rel}$	$\Delta T_{rel,max}$
C01	Charge	180 °C – 380 °C	0.06	−5.8 % (−8.1 % to −3.1 %)	−12.3 % (−17.7 % to −6.3 %)
C02	Charge	180 °C – 380 °C	0.16	−4.3 % (−6.6 % to −2.0 %)	−6.6 % (−9.3 % to −4.5 %)
C03	Charge	180 °C – 380 °C	0.16	−5.1 % (−7.5 % to −2.6 %)	−7.2 % (−10.3 % to −4.6 %)
C04	Charge	180 °C – 380 °C	0.24	−4.5 % (−7.0 % to −2.0 %)	−6.9 % (−10.6 % to −4.2 %)
C05	Charge	180 °C – 380 °C	0.31	−4.9 % (−7.5 % to −2.2 %)	−7.8 % (−11.7 % to −4.7 %)
C06	Charge	180 °C – 250 °C	0.31	−5.7 % (−8.0 % to −3.5 %)	−9.4 % (−12.4 % to −7.9 %)
C07	Charge	200 °C – 270 °C	0.12	−6.2 % (−8.1 % to −4.3 %)	−8.2 % (−10.5 % to −6.3 %)
C08	Charge	200 °C – 270 °C	0.13	−6.1 % (−8.0 % to −4.1 %)	−8.1 % (−10.4 % to −6.2 %)
C09	Charge	200 °C – 270 °C	0.24	−7.3 % (−9.5 % to −5.0 %)	−10.7 % (−13.7 % to −8.2 %)
C10	Charge	200 °C – 270 °C	0.24	−7.6 % (−9.9 % to −5.4 %)	−11.2 % (−14.2 % to −8.6 %)
C11	Charge	200 °C – 270 °C	0.32	−8.6 % (−11.0 % to −6.2 %)	−13.0 % (−16.5 % to −10.2 %)
D01	Discharge	180 °C – 380 °C	0.06	2.8 % (0.0 % to 5.4 %)	8.0 % (−2.2 % to 14.0 %)
D02	Discharge	180 °C – 380 °C	0.12	2.0 % (−0.6 % to 4.4 %)	2.9 % (−2.7 % to 6.0 %)
D03	Discharge	180 °C – 380 °C	0.12	2.7 % (0.1 % to 5.2 %)	3.7 % (−2.2 % to 7.6 %)
D04	Discharge	180 °C – 380 °C	0.16	2.3 % (−0.2 % to 4.7 %)	3.6 % (−1.8 % to 6.8 %)
D05	Discharge	180 °C – 380 °C	0.16	3.1 % (0.6 % to 5.7 %)	4.5 % (1.6 % to 7.9 %)
D06	Discharge	180 °C – 380 °C	0.23	1.7 % (−0.9 % to 4.2 %)	2.7 % (−2.6 % to 6.5 %)
D07	Discharge	180 °C – 380 °C	0.24	1.6 % (−1.0 % to 4.1 %)	2.7 % (−2.6 % to 6.3 %)
D08	Discharge	180 °C – 380 °C	0.31	2.3 % (−0.3 % to 4.9 %)	3.7 % (−1.7 % to 8.2 %)
D09	Discharge	180 °C – 380 °C	0.31	3.3 % (0.6 % to 5.9 %)	5.2 % (1.8 % to 9.8 %)
D10	Discharge	180 °C – 250 °C	0.31	2.5 % (0.3 % to 4.6 %)	4.2 % (3.2 % to 7.6 %)
D11	Discharge	200 °C – 270 °C	0.06	1.2 % (−1.1 % to 3.2 %)	2.8 % (−5.0 % to 6.3 %)
D12	Discharge	200 °C – 270 °C	0.06	1.5 % (−0.8 % to 3.7 %)	3.1 % (−4.7 % to 8.4 %)
D13	Discharge	200 °C – 270 °C	0.12	2.3 % (0.3 % to 4.2 %)	3.7 % (2.8 % to 5.8 %)
D14	Discharge	200 °C – 270 °C	0.24	2.9 % (0.9 % to 4.9 %)	4.9 % (3.4 % to 7.8 %)
D15	Discharge	200 °C – 270 °C	0.24	2.9 % (0.9 % to 5.0 %)	4.9 % (3.4 % to 7.9 %)
D16	Discharge	200 °C – 270 °C	0.31	3.5 % (1.4 % to 5.7 %)	5.9 % (4.2 % to 9.3 %)
D17	Discharge	200 °C – 270 °C	0.32	3.6 % (1.6 % to 5.8 %)	6.0 % (4.2 % to 9.5 %)

4.3. Discussion

In the following, the discrepancies between the simulation and the experimental data are discussed and the impact of key simplifications are evaluated.

4.3.1. Differences between simulation of charging and discharging behavior

The differences between the discharging and charging experiments described in Section 4.2 can presumably be explained by an inhomogeneous temperature distribution at the upper inlet. Potential causes for this could be an insufficiently homogeneous distribution of the incoming fluid at the upper flange or inadequate sealing between the sintered filter and the inserted thermocouple lance. As a result, the inlet temperature would be overestimated in the simulation, leading to the observed deviations. This assumption is supported by the observation that during the charging experiments, the temperature measured by a thermocouple attached directly to the sintered filter at the top is several Kelvin lower than the temperature measured by the topmost thermocouple on the vertical lance. The latter sensor is positioned directly downstream of the sintered filter. Normally, the opposite would be expected in charging experiments. The temperature difference between these two sensors is larger than can be explained by measurement uncertainties. This anomaly is not observed in the discharge experiments.

Moreover, the energy balance in the charging experiments, which is determined using the measured temperatures, shows some discrepancies. The supplied enthalpy flow, determined from the measured inlet temperatures and accounting for heat losses to the surroundings, is 6 % larger than the enthalpy change in the storage for experiment C05. For the corresponding discharge experiment D08, however, the discrepancy is only 2.8 %. Since the charging and discharging experiments were conducted within the same temperature range, uncertainties in material properties data, which are also considered in the Monte Carlo simulation, can be excluded as a potential cause for the higher deviation of the charging experiments, as this would affect both charging and discharging in the same way. An incorrect description of axial heat dispersion is also not a plausible cause for the observed deviation, as this would only lead to a change in the slope of the temperature profile. The energy balance, however, remains unaffected by this.

4.3.2. Influence of outlet boundary condition and heat loss

While the selected outlet condition and the accounted heat loss to the ambient have little impact on the simulation results in the cases shown in Figs. 6 and 7, they do affect experiments that fall in the lower end of the investigated Péclet number range. With decreasing Péclet number the discharging/charging takes significantly longer. As a consequence, the effects of heat loss to the ambient are significantly more pronounced. Fig. 8 shows that, for $Pe_0 \approx 0.06$, the outlet temperature of the TES system decreases even though the thermocline has not yet reached the outlet. This can be recognized by the fact that the outlet temperature decreases, without any change in the gradient of the measured temperature profile in the upper part of the TES. After 2035 s, the measured temperature at the outlet ($x = 0.369$ m) is already 9 K lower than the initial temperature. However, the simulation appears to be able to represent the heat losses to the surroundings with sufficient accuracy, despite the assumption of a homogeneous temperature profile on the outer side of the insulation (see Section 4).

As Fig. 8 also shows, the low flow velocity ($u_\epsilon \approx 0.4\,\mathrm{mm\,s^{-1}}$) at $Pe_0 \approx 0.06$ causes the thermocline to extend across nearly the entire width of the TES system, which can be recognized by the fact that the target temperature of 180 °C has not yet been reached at the inlet and a pronounced gradient in the measured temperature profile is observed at the outlet after 4071 s, which cannot be explained solely by heat losses to the surroundings. This means that the thermocline reaches the outlet during the experiment. Since the storage was charged and discharged only up to half of its capacity, this was not the case in the experiments at higher Péclet numbers. The measurement data indicate that the assumption of a zero heat flux at the outlet does not represent the real system. This leads to significant deviations between the calculated and measured outlet temperatures. To investigate the influence of the boundary condition, Fig. 8 also includes a simulation in which the packed bed is assumed to be 20 cm longer. In the specific case shown, the mean relative deviation is thereby reduced by

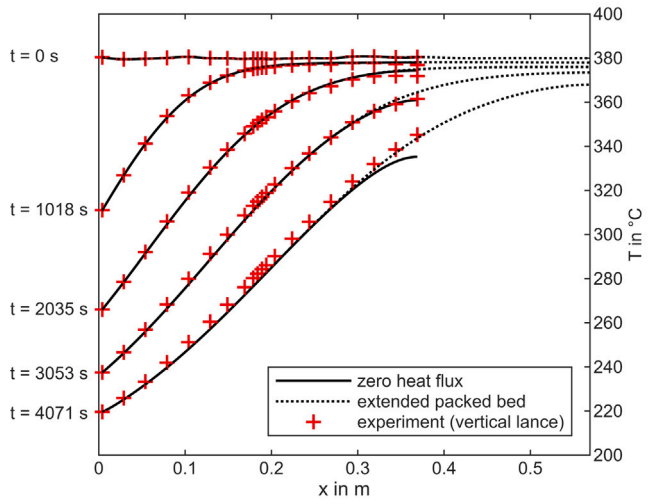

Fig. 8. Simulated and measured temperature profiles of experiment D01 at various points in time. Shown are the results of the simulation using a zero heat flux as the outlet condition and a simulation with the packed bed extended by 20 cm. For clarity, the 95 % confidence of the simulation interval is not shown.

approximately 1.1 percentage points. However, the effect of the chosen boundary condition on the simulation appears to be limited to a region within approximately 10 cm of the outlet.

The boundary condition may also be the reason for the notably high maximum relative deviation observed in experiment C01. By applying the extended packed bed condition, the maximum relative deviation is halved, lowering it to around 5.7 %.

4.3.3. Dependence on Péclet number and temperature level

The observed linear dependence of the mean relative deviation on the Péclet number at a temperature level of 200 °C to 270 °C may have several causes. It is possible that the actual effective thermal conductivity increasingly deviates from the effective thermal conductivity calculated using Eq. (7) as the Péclet number, and thus the turbulence, increases (see Section 2.2). However, a significantly greater effect is likely due to the fact that the radial temperature profile also increases with rising Péclet number, which is measured by the horizontal thermocouple at one level in the tank. Since the simulation is one-dimensional, a radially averaged temperature is calculated, which increasingly deviates from the temperatures measured in the center as the radial temperature profile becomes more pronounced.

However, these effects appear to be superimposed by other phenomena in the experiments with higher temperature differences (180 °C to 380 °C), so that no dependence on the Péclet number can be observed. Possible superimposing effects could include an insufficient representation of heat loss to the ambient, which becomes more pronounced at higher temperatures. In general, larger relative deviations between simulations and experiments are expected for experiments with smaller temperature spread in the TES system. This is because inaccuracies that are independent of temperature ranges, such as uncertainties in the mass flow measurement or an inhomogeneous temperature distribution at the inlet, have a proportionally stronger effect on the relative deviation when the reference temperature spread is smaller.

4.3.4. Influence of assuming single-sphere heat transfer coefficient and neglecting internal temperature gradients

Despite the small particle diameter, the Biot number ($\mathrm{Bi} = \alpha d_\mathrm{p}/(2\lambda_\mathrm{p})$) is between 1.8 and 2 due to the large heat transfer coefficient. This would indicate that the thermal conductivity within the particles and the heat transfer between particles and fluid need to be considered. However, in this context, the Biot number is of limited significance because it accounts only for the heat transfer and intra-particle heat conduction, but not for the axial heat transport in the packed bed, which dominates in the considered Péclet number range.

The simplification that the Nusselt number is calculated using the correlation for a single sphere, or is set to 2 for flow velocities outside the defined range of the applied correlation, has no relevant impact on the simulation results. The temperature difference between the fluid and the particle temperature is negligibly small for all investigated experiments. This means that the heat transfer between particles and fluid is not limiting. A higher Nusselt number, which is to be expected in a packed bed, would therefore have no significant effect on the calculations carried out here.

Neglecting the temperature gradient within the particles also has no significant impact on the calculations. To verify this, a discharge experiment at a Péclet number of 0.31 (experiment D08), which lies at the upper end of the investigated Péclet number range, was examined. The maximum temperature difference between the particle surface and the core of the particle was less than 0.14 K. This only affects the second decimal place in the calculation of the mean relative deviations at the end of the experiment. For experiments at lower Péclet numbers, the temperature gradient within the particles decreases further. The assumption that the temperature gradient within the particles is negligible in the lab-scale experiment is therefore justified and in good agreement with the considerations presented in Section 2.3.

4.4. Key findings

Overall, the results show that the model presented in Section 3 allows for highly accurate calculation of the thermocline propagation during charging and discharging of a TES when using liquid metals as HTF for Péclet numbers up to at least 0.32. The absolute values of the relative mean deviations from the experimental data are very small for discharging processes (less than 3.6 %). Since the experimentally determined values during discharging lie mostly within the 95 % confidence interval of the simulation, the remaining discrepancies appear to be mainly attributable to uncertainties in the material properties data and measured input parameters. The most important heat transport parameters seem to be sufficiently well accounted for. The larger relative deviations observed during charging processes (up to 5.8 % for a temperature spread of 200 K and up to 8.6 % for a temperature spread of 70 K) are presumably due to insufficient mixing at the inlet, resulting in an inhomogeneous temperature distribution.

At the low Péclet numbers investigated here, intra-particle heat conduction and heat transfer between particles and fluid make a minor contribution to the overall heat dispersion. Neglecting the temperature gradient inside the particles and using the Nusselt correlation for a single sphere in crossflow, or applying $\mathrm{Nu} = 2$, is therefore justified. Furthermore, the considerations from Section 2.4 can be confirmed. Due to the low Péclet numbers, the effective thermal conductivity is primarily dominated by molecular heat conduction, and Eq. (7) can be applied.

Heat loss to the ambient becomes relevant especially during longer charging/discharging durations and can also be represented with sufficient accuracy. Moreover, in cases, in which the realized temperature step reached the outlet, larger deviations between simulation and experiment were observed. These larger deviations can mainly attributed to an insufficient representation of the boundary condition at the outlet, which, is limited to a region within approximately 10 cm of the outlet. However, for TES systems with commercially usable dimensions and several meters in height, the outlet boundary condition is likely to have a negligibly small influence on the calculated thermocline propagation.

5. Simulation of packed-bed TES systems with liquid metals as HTF at moderate Péclet numbers

As already discussed in Section 2.4, the determination of axial heat transport at higher Péclet numbers (when the turbulent mixing of the fluid becomes more important) is associated with considerable uncertainties for liquid metals. In this case, the effective thermal conductivity is unknown. Furthermore, as previously mentioned, to date only a minimum Nusselt number can be specified for a packed bed with a liquid metal flow. However, as outlined in Section 2.3, axial heat transport is likely the dominant mechanism, yet the contribution of heat transfer between particles and fluid cannot be neglected. Therefore, in the following, the sensitivity of the simulation to the effective thermal conductivity and the Nusselt number will be examined in more detail. As a reference case, the heat transfer coefficient between fluid and particles is determined using Eq. (6) for a single sphere and Eq. (7) is used to calculate the effective thermal conductivity.

The Nusselt number of a single sphere in crossflow represents a minimal Nusselt number for a packed bed with fluid flow. Gnielinski [29] proposed extending his correlation for a single sphere to a packed bed by multiplying the single-sphere correlation with a shape factor. This shape factor f_a depends solely on the porosity of the packed bed ϵ and can be calculated using Eq. (23).

$$f_a = 1 + 1.5\,(1 - \epsilon) \tag{23}$$

The application of the shape factor in combination with Eq. (6) has not yet been validated, but is used here to estimate the influence of the packed bed. Assuming a porosity of 36 %, this corresponds to nearly a doubling of the heat transfer coefficient for a packed bed compared to a single sphere. Furthermore, the simulation is performed with the effective thermal conductivity increased and decreased by 50 %, respectively.

For the analysis, the pilot-scale TES currently being constructed at KALLA, with a total height of 1.98 m, serves as an example of a TES system operating at moderate Péclet numbers. Similar to the lab-scale experiment, 2.65 mm zirconium silicate spheres are used as the storage material, and lead-bismuth eutectic is again used as the model HTF. The investigation is performed at a Péclet number of 5. This corresponds to the maximum Péclet number in the planned pilot-scale experiment and is also the range in which the greatest uncertainty in the simulation of axial heat dispersion is expected (see Fig. 3). As shown in Fig. 5, intra-particle heat conduction has a non-negligible influence on axial heat dispersion at this Péclet number and is therefore taken into account.

5.1. Impact of uncertainties in heat transport correlations on pilot-scale TES simulation

Fig. 9 shows the simulated temperature profiles at the outlet of the pilot-scale TES unit. It is clearly visible that the introduction of the shape factor has only a minor impact on the calculated outlet temperature profile. The maximum deviation from the reference simulation is less than 2.5 K. In contrast, the sensitivity study shows that uncertainties in the determination of the effective thermal conductivity have a greater impact. An increase in the effective thermal conductivity by 50 % leads to deviations from the reference simulation of up to 8.4 K. If the effective thermal conductivity is reduced by 50 %, the deviation even increases to up to 11.8 K.

5.2. Key findings

Although the uncertainty in the determination of the heat transfer coefficient between fluid and particles is high, it has only a minor impact on the simulation of the thermocline propagation. The correlation for a single sphere allows at least the calculation of a minimal Nusselt number. Furthermore, because of the high thermal conductivity of liquid metals, heat transfer is very efficient and therefore not limiting.

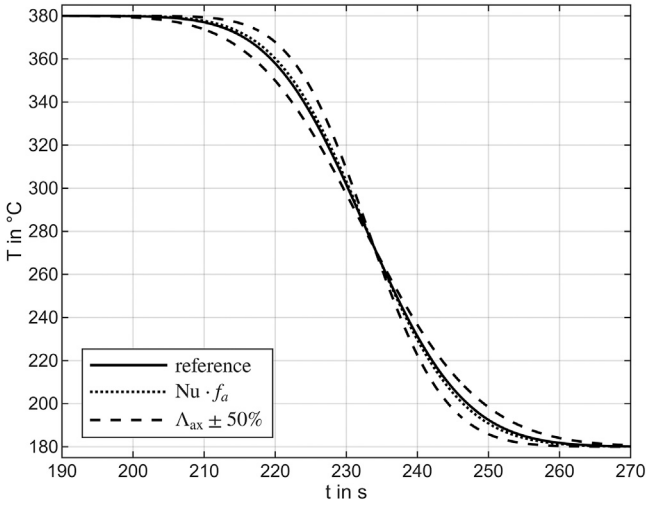

Fig. 9. Simulated temperature profiles at the outlet of the pilot-scale TES with $Pe_0 = 5$ under discharging condition. The reference simulation is carried out with Eq. (7) for the effective thermal conductivity and the Nusselt correlation for the single sphere (Eq. (6)). For comparison, the simulation is performed with the effective thermal conductivity reduced and increased by ± 50 % (dashed). In the dotted case, the Nusselt number for a single sphere is multiplied by the shape factor given in Eq. (23).

Consequently, the contribution of heat transfer to the overall axial heat dispersion, and thus to the diffusive propagation of the thermocline, is relatively small. The observations are in good agreement with the considerations in Section 2.3. In contrast, the unknown effective thermal conductivity of liquid metals in the investigated moderate Péclet number range leads to considerable deviations in the calculation of the diffusive propagation of the thermocline. Therefore, accurate quantitative analyses with Eq. (7) are not possible. Especially in studies involving multiple charging and discharging cycles, the uncertainty would accumulate. As a result, a targeted design or optimization of the TES systems at moderate Péclet numbers is not feasible yet.

6. Conclusion

In packed-bed TES systems using liquid metals as the HTF, the axial heat transport, described by the effective thermal conductivity, can be estimated as the dominant heat-transport mechanism. The effective thermal conductivity accounts for molecular heat conduction in both the solid and fluid phases as well as heat transport due to turbulent mixing. In contrast, heat transfer between particles and fluid, and intra-particle heat conduction, make only a minor contribution to the overall axial heat dispersion and therefore to the diffusive propagation of the thermocline during charging and discharging of the TES system.

At low Péclet numbers, axial heat transport is likely dominated by molecular heat conduction. In this regime, the effective thermal conductivity can be calculated using models that have been established for thermal conductivity in a porous media with stagnant fluid flow. To demonstrate this, an existing one-dimensional heterogeneous continuum model with a dispersed solid phase was extended. Moreover, it could be shown that an estimation of the heat transfer coefficient between particles and fluid using a correlation for single spheres is sufficient. This estimation is necessary because, to the best of the authors' knowledge, no correlation for the heat transfer coefficient of a packed bed in the low Prandtl number region for liquid metals has been validated.

With the developed model, the lab-scale experiment conducted by Müller-Trefzer et al. [16] using LBE as the model HTF could be accurately simulated for the first time, thus validating the simulation

for Péclet numbers up to 0.32. For discharge experiments, the mean relative deviation between simulation and experiment is maximal 3.6 %. For charge experiments, the absolute mean relative deviation is higher, reaching 8.6 %. The larger deviation in the charge experiments is likely primarily due to an inhomogeneous temperature distribution at the upper inlet of the experiment, which cannot be accounted for in the simulation.

However, as the Péclet number increases, the influence of turbulent mixing of the fluid on axial heat transport becomes more significant. To the best of the authors' knowledge, no validated equation exists for calculating the effective thermal conductivity in this regime for liquid metals. Due to the very low Prandtl number of liquid metals, the heat transport phenomena differ significantly from those of conventional fluids, and correlations developed for conventional fluids cannot be used. Since axial heat transport is the dominant mechanism of axial heat dispersion in the relevant Péclet number range of TES systems, the uncertainty in calculating the effective thermal conductivity has a considerable impact. Therefore, reliable design and optimization of TES systems at moderate Péclet numbers is currently not possible. To achieve this, further research into the effective thermal conductivity of packed beds with a liquid metal flow is required.

CRediT authorship contribution statement

Eike A. Schmidt: Conceptualization, Methodology, Software, Validation, Formal analysis, Visualization, Writing – original draft. **Thomas Wetzel:** Supervision, Writing – review & editing. **Klarissa Niedermeier:** Supervision, Methodology, Funding acquisition, Writing – review & editing.

Declaration of Generative AI and AI-assisted technologies in the writing process

During the preparation of this work the authors used Microsoft 365 Copilot and DeepL for translation and to improve readability. After using this tool/service, the authors reviewed and edited the content as needed and take full responsibility for the content of the published article.

Declaration of competing interest

The authors declare that they have no known competing financial interests or personal relationships that could have appeared to influence the work reported in this paper.

Acknowledgments

This research was funded by the Deutsche Forschungsgemeinschaft (DFG, German Research Foundation), Germany – grant number 52615 2734 within the framework of the DFG priority programme SPP 2403 "Carnot Batteries: Inverse Design from Markets to Molecules". The authors thank the DFG for the financial support. Additionally, the authors acknowledge support by the state of Baden-Württemberg through bwHPC. Furthermore, the authors wish to thank Franziska Müller-Trefzer for her consultation regarding the lab-scale experiment.

Data availability

Data will be made available on request.

References

[1] W.-D. Steinmann, H. Jockenhöfer, D. Bauer, Thermodynamic analysis of high-temperature carnot battery concepts, Energy Technol. 8 (3) (2020) 1900895, http://dx.doi.org/10.1002/ente.201900895.
[2] T. Liang, A. Vecchi, K. Knobloch, A. Sciacovelli, K. Engelbrecht, Y. Li, Y. Ding, Key components for carnot battery: Technology review, technical barriers and selection criteria, Renew. Sustain. Energy Rev. 163 (2022) 112478, http://dx.doi.org/10.1016/j.rser.2022.112478.
[3] J.E. Pacheco, S.K. Showalter, W.J. Kolb, Development of a molten-salt thermocline thermal storage system for parabolic trough plants, J. Sol. Energy Eng. 124 (2) (2002) 153–159, http://dx.doi.org/10.1115/1.1464123.
[4] H. Bindra, P. Bueno, J.F. Morris, R. Shinnar, Thermal analysis and exergy evaluation of packed bed thermal storage systems, Appl. Therm. Eng. 52 (2) (2013) 255–263, http://dx.doi.org/10.1016/j.applthermaleng.2012.12.007.
[5] A. Bruch, J. Fourmigué, R. Couturier, Experimental and numerical investigation of a pilot-scale thermal oil packed bed thermal storage system for CSP power plant, Sol. Energy 105 (2014) 116–125, http://dx.doi.org/10.1016/j.solener.2014.03.019.
[6] F. Dinter, D.M. Gonzalez, Operability, reliability and economic benefits of CSP with thermal energy storage: First year of operation of ANDASOL 3, Energy Procedia 49 (2014) 2472–2481, http://dx.doi.org/10.1016/j.egypro.2014.03.262, Proceedings of the SolarPACES 2013 International Conference.
[7] G. Alva, Y. Lin, G. Fang, An overview of thermal energy storage systems, Energy 144 (2018) 341–378, http://dx.doi.org/10.1016/j.energy.2017.12.037.
[8] B. Pomeroy, Thermal energy storage in a packed bed of iron spheres with liquid sodium coolant, Sol. Energy 23 (6) (1979) 513–515, http://dx.doi.org/10.1016/0038-092X(79)90075-6.
[9] C. Forsberg, Separating nuclear reactors from the power block with heat storage to improve economics with dispatchable heat and electricity, Nucl. Technol. 208 (4) (2022) 688–710, http://dx.doi.org/10.1080/00295450.2021.1947121.
[10] M.V. Bozorg, J. Coventry, J.F. Torres, Thermal energy storage in a tightly packed bed with sodium as the heat transfer fluid: A numerical study, Appl. Energy 352 (2023) 121879, http://dx.doi.org/10.1016/j.apenergy.2023.121879.
[11] K. Niedermeier, A perspective on high-temperature heat storage using liquid metal as heat transfer fluid, Energy Storage 5 (8) (2023) e530, http://dx.doi.org/10.1002/est2.530.
[12] J. Pacio, C. Singer, T. Wetzel, R. Uhlig, Thermodynamic evaluation of liquid metals as heat transfer fluids in concentrated solar power plants, Appl. Therm. Eng. 60 (1) (2013) 295–302, http://dx.doi.org/10.1016/j.applthermaleng.2013.07.010.
[13] J. Pacio, T. Wetzel, Assessment of liquid metal technology status and research paths for their use as efficient heat transfer fluids in solar central receiver systems, Sol. Energy 93 (2013) 11–22, http://dx.doi.org/10.1016/j.solener.2013.03.025.
[14] T. Laube, L. Marocco, K. Niedermeier, J. Pacio, T. Wetzel, Thermodynamic analysis of high-temperature energy storage concepts based on liquid metal technology, Energy Technol. 8 (3) (2020) 1900908, http://dx.doi.org/10.1002/ente.201900908.
[15] K. Niedermeier, L. Marocco, J. Flesch, G. Mohan, J. Coventry, T. Wetzel, Performance of molten sodium vs. molten salts in a packed bed thermal energy storage, Appl. Therm. Eng. 141 (2018) 368–377, http://dx.doi.org/10.1016/j.applthermaleng.2018.05.080.
[16] F. Müller-Trefzer, K. Niedermeier, M. Daubner, T. Wetzel, Experimental investigations on the design of a dual-media thermal energy storage with liquid metal, Appl. Therm. Eng. 213 (2022) 118619, http://dx.doi.org/10.1016/j.applthermaleng.2022.118619.
[17] E.A. Schmidt, F. Müller-Trefzer, M. Daubner, T. Wetzel, K. Niedermeier, Experimental data from a packed-bed thermal energy storage system using liquid metal as heat transfer fluid during charging and discharging, 2026, http://dx.doi.org/10.35097/byayp53e2q6ns3z3.
[18] F. Müller-Trefzer, A. Heinzel, R. Hesse, A. Weisenburger, T. Wetzel, K. Niedermeier, Screening of filler material for a packed-bed thermocline energy storage test facility with lead–bismuth eutectic as the heat transfer fluid, Energy Technol. 12 (2) (2024) 2300781, http://dx.doi.org/10.1002/ente.202300781.
[19] M. Zehnder, A. Purwitasari, A. Heinzel, K. Niedermeier, Study on corrosion and thermal alteration of low-cost storage materials for use in high-temperature thermal energy storage systems with lead as the heat transfer fluid, Energy Storage 7 (8) (2025) e70305, http://dx.doi.org/10.1002/est2.70305, e70305 9475565.
[20] K. Niedermeier, M. Lux, A. Purwitasari, A. Weisenburger, M. Daubner, F. Müller-Trefzer, T. Wetzel, Design of the LIMELIGHT test rig for component testing for high-temperature thermal energy storage with liquid metals, Processes 11 (10) (2023) http://dx.doi.org/10.3390/pr11102975.
[21] M. Kaviany, Principles of heat transfer in porous media, second ed., in: Mechanical engineering series, Springer, New York, 1995.
[22] E. Tsotsas, M7 Wärmeleitung und Dispersion in durchströmten Schüttungen, in: P. Stephan, S. Kabelac, M. Kind, D. Mewes, K. Schaber, T. Wetzel (Eds.), VDI-Wärmeatlas: Fachlicher Träger VDI-Gesellschaft Verfahrenstechnik Und Chemieingenieurwesen, Springer Berlin Heidelberg, Berlin, Heidelberg, 2019, pp. 1753–1772, http://dx.doi.org/10.1007/978-3-662-52989-8_102.

[23] C. Stegehake, J. Riese, M. Grünewald, Aktueller Stand zur Modellierung von Festbettreaktoren und Möglichkeiten zur experimentellen Validierung, Chem. Ing. Tech. 90 (11) (2018) 1739–1758, http://dx.doi.org/10.1002/cite.201800130.
[24] N. Wakao, S. Kaguei, Heat and mass transfer in packed beds, in: Topics in chemical engineering, Gordon and Breach, New York [u.a.], 1982.
[25] E. Tsotsas, Über die Wärme- und Stoffübertragung in durchströmten Festbetten, in: Fortschritt-Berichte VDI, VDI-Verl., Düsseldorf, 1990.
[26] NEA, Handbook on lead-bismuth eutectic alloy and lead properties, materials compatibility, thermalhydraulics and technologies, in: Nuclear Science, OECD Publishing, Paris, 2015, http://dx.doi.org/10.1787/42dcd531-en.
[27] B. Melissari, S.A. Argyropoulos, Development of a heat transfer dimensionless correlation for spheres immersed in a wide range of Prandtl number fluids, Int. J. Heat Mass Transfer 48 (21) (2005) 4333–4341, http://dx.doi.org/10.1016/j.ijheatmasstransfer.2005.05.025.
[28] G. Ahmed, M. Yovanovich, Approximate analytical solution of forced convection heat transfer from isothermal spheres for all Prandtl numbers, J. Heat Transfer-Transactions the Asme - J HEAT TRANSFER 116 (1994) http://dx.doi.org/10.1115/1.2911456.
[29] V. Gnielinski, G9 Wärmeübertragung bei erzwungener Konvektion: Durchströmte Haufwerke, in: P. Stephan, S. Kabelac, M. Kind, D. Mewes, K. Schaber, T. Wetzel (Eds.), VDI-Wärmeatlas: Fachlicher Träger VDI-Gesellschaft Verfahrenstechnik Und Chemieingenieurwesen, Springer Berlin Heidelberg, Berlin, Heidelberg, 2019, pp. 889–891, http://dx.doi.org/10.1007/978-3-662-52989-8_50.
[30] E. Skupinski, J. Tortel, L. Vautrey, Determination des coefficients de convection d'un alliage sodium-potassium dans un tube circulaire, Int. J. Heat Mass Transfer 8 (6) (1965) 937–951, http://dx.doi.org/10.1016/0017-9310(65)90077-3.
[31] T. Laube, B. Dietrich, L. Marocco, T. Wetzel, Turbulent heat transfer in a liquid metal tube flow with azimuthally inhomogeneous heat flux, Int. J. Heat Mass Transfer 189 (2022) 122734, http://dx.doi.org/10.1016/j.ijheatmasstransfer.2022.122734.
[32] E. Tsotsas, M11 Wärmeleitfähigkeit von Schüttschichten, in: P. Stephan, S. Kabelac, M. Kind, D. Mewes, K. Schaber, T. Wetzel (Eds.), VDI-Wärmeatlas: Fachlicher Träger VDI-Gesellschaft Verfahrenstechnik Und Chemieingenieurwesen, Springer Berlin Heidelberg, Berlin, Heidelberg, 2019, pp. 1831–1843, http://dx.doi.org/10.1007/978-3-662-52989-8_30.
[33] R. Aris, N.R. Amundson, Some remarks on longitudinal mixing or diffusion in fixed beds, AIChE J. 3 (2) (1957) 280–282, http://dx.doi.org/10.1002/aic.690030226.
[34] J. Delgado, Longitudinal and transverse dispersion in porous media, Chem. Eng. Res. Des. 85 (9) (2007) 1245–1252, http://dx.doi.org/10.1205/cherd07017.
[35] E. Tsotsas, E. Schlünder, On axial dispersion in packed beds with fluid flow: Über die axiale Dispersion in durchströmten Festbetten, Chem. Eng. Process.: Process. Intensif. 24 (1) (1988) 15–31, http://dx.doi.org/10.1016/0255-2701(88)87002-8.
[36] Joint Committee for Guides in Metrology (JCGM), Evaluation of measurement data — Guide to the expression of uncertainty in measurement, 2008, http://dx.doi.org/10.59161/JCGM100-2008E.
[37] M. Matus, Koeffizienten und Ausgleichsrechnung: Die Messunsicherheit nach GUM. Teil 1: Ausgleichsgeraden (Coefficients and Adjustment Calculations: Measurement Uncertainty under GUM. Part 1: Best Fit Straight Lines), Tm - Tech. Mess. 72 (10) (2005) 584–591, http://dx.doi.org/10.1524/teme.2005.72.10_2005.584.
[38] C. Ullrich, T. Bodmer, D6.1 Thermophysikalische Stoffwerte von Metallen und Metalllegierungen, in: P. Stephan, S. Kabelac, M. Kind, D. Mewes, K. Schaber, T. Wetzel (Eds.), VDI-Wärmeatlas: Fachlicher Träger VDI-Gesellschaft Verfahrenstechnik Und Chemieingenieurwesen, Springer Berlin Heidelberg, Berlin, Heidelberg, 2019, pp. 645–658, http://dx.doi.org/10.1007/978-3-662-52989-8_28.
[39] ABRAMS Industries Inc., 316Ti Datasheet, 2012, ABRAMS Industries, 2012.
[40] SAINT-GOBAIN ISOVER G+H AG, TECH Wired Mat 4.3 MD – Technisches Datenblatt, 2025, Stand: 19.05.2025.